564324

SEGMENTED DOMAIN DECOMPOSITION MULTIGRID FOR 3-D TURBOMACHINERY FLOWS

M. L. Celestina
A.P. Solutions, Inc.

J. J. Adamczyk
NASA Glenn Research Center

S. G. Rubin
University of Cincinnati

ABSTRACT

A Segmented Domain Decomposition Multigrid (SDDMG) procedure was developed for three-dimensional viscous flow problems as they apply to turbomachinery flows. The procedure divides the computational domain into a coarse mesh comprised of uniformly spaced cells. To resolve smaller length scales such as the viscous layer near a surface, segments of the coarse mesh are subdivided into a finer mesh. This is repeated until adequate resolution of the smallest relevant length scale is obtained. Multigrid is used to comunicate information between the different grid levels. To test the procedure, simulation results will be presented for a compressor and turbine cascade. These simulations are intended to show the ability of the present method to generate grid independent solutions. Comparisons with data will also be presented. These comparisons will further demonstrate the usefulness of the present work for they allow an estimate of the accuracy of the flow modeling equations independent of error attributed to numerical discretization.

INTRODUCTION

To maintain a reasonable number of mesh points while attempting to resolve the wide range of length scales associated with turbomachinery passage flows, mesh stretching is often employed. However, mesh stretching can have an adverse effect on the convergence rate of a solution. This is particularly true if large mesh stretching is used. Another issue which impacts the convergence rate of finite volume discretization formulations is the ratio of the largest surface area of a cell to the smallest surface area of a cell. This ratio is often referred to as cell aspect ratio. It is well known that large values of cell aspect ratio can severely compromise the solution convergence rate.

Code developers, from experience or analysis, [Celestina, 1999], developed rules which govern the range of mesh stretching of cell aspect ratio to be used with their codes. Users are strongly encouraged to follow these rules in order to attain solution convergence. However, in some applications, strict adherance to the rules is not sufficient to ensure solution convergence nor does it guarantee adequate resolution of flow details.

The motivation for the present work came from attempts at developing a single mesh which is sufficiently fine to accurately capture a number of key flow features which are known to impact the aerodynamic performance of turbomachinery blading. This task becomes quite difficult if the mesh is required to conform to the stretching and aspect ratio rules and the number of mesh points or mesh cells are being held constant in order to control solution times.

This difficulty associated with stretched meshes led to an investigation of alternative meshing strategies. A promising mesh generation strategy which can overcome the stated difficutly is based on a mesh patch strategy known as domain decomposition. Domain decomposition employs a number of mesh segmented domains ,i.e., mesh patches, which may or may not overlap. The mesh in each segmented domain is tailored so as to capture the dominant flow features within the domain. Some examples of works in this area are papers by Berger *et al.* [1989]. Another is the CHIMERA method originally developed by Steger *et al.* [1987] and sinced refined by Liu [1994].

Brandt [1977] observed that certain forms of domain decomposition can be viewed in the context of a multigrid solution strategy. These particular types of domain decomposition use a multigrid procedure to communicate information between the various mesh patches. The resulting methodology is called Segmented Domain Decomposition

Multigrid Strategy (SDDMG).

The first implementation of a SDDMG procedure to internal flows was by Srinivasan and Rubin [1997]. They developed an adaptive approach to achieve optimal mesh resolution of a number of internal flows. Their work showed that the SDDMG method improved the resolution of the flowfield throughout as compared to a solution obtained with a single mesh using the same number of mesh pionts.

The objective of this work is to develop a Segmented Domain Decomposition Multigrid Strategy within the framework of a three-dimensional finite volume, cell-centered scheme which solves the Reynolds-Averaged form of the Navier-Stokes equations for turbomachinery flows. A key objective being the capability to efficiently generate solutions which are mesh independent. The strategy is to use uniform meshes in the blade-to-blade direction. For a three dimensional simulation, a stretched mesh is used in the span-wise direction. The uses of a stretched mesh in the spanwise direction allowed a straight forward assessemt of the usefulness of the SSMG procedure prior to a full 3D implementation.

The main elements of the SDDMG procedure are: a multiblock structure; a multigrid strategy; a mesh generation procedure; boundary conditions; and interface conditions.

The next section discusses the above elements in more detail. The SDDMG method is then applied to two cases. The first is a compressor cascade and the second is a turbine cascade. The intent of these simulations is to show the ability of the SDDMG method to converge to the underlying flow features which control the aerodynamic performance of turbomachinery blade rows. Where applicable the simulation results are compared to measurements. The final section presents a summary of this work with conclusions based on the results.

PROCEDURE

The SDDMG procedure solves the Reynolds-averaged Navier-Stokes equations, i.e., mean flow equations, using a cell-centered finite volume formulation. On each mesh, a Runge-Kutta iteration procedure is used to advance the solution [Adamczyk, *et al.* 1990].

The present work uses the two-equation standard $k-\epsilon$ turbulence model of Launder and Spalding [1974] to estimate the eddy viscosity. This turbulence model is a high Reynolds number model which requires the use of wall functions at solid surfaces and is valid from the outer region of a turbulent boundary layer to the beginning of the log-layer.

The k and ϵ equations are discretized in the same way as the governing mean flow equations. The details of the discretization can be found in Shabbir, *et al.* [1996].

A mesh generation code developed by Mulac [1986] generated all of the meshes used in this work. The code is a general purpose turbomachinery mesh generator which generates a three-dimensional H-mesh by applying a series of cubic spline fits to the geometric definition of the flowpath and blade.

The elements necessary to develop and implement a domain decomposition strategy for a general, three-dimensional rotating turbomachine are: a multiblock flow solver; a multigrid solution strategy; a multiblock mesh generation strategy; a boundary condition strategy compatible with a multiblock flow solver; and interface conditions compatible with a multiblock flow solver.

Multiblock Structure. The multiblock structure for the current work begins with a single global parent mesh. This mesh is comprised of uniform cells and covers the entire computational domain. A global parent mesh is shown in Figure 1 in computational space.

The first level of refinement subdivides the global parent mesh into sub-domain meshes. These segmented domains, relative to the global parent mesh, are called child meshes. The only rule that must be followed in refining a mesh level is that the boundary mesh lines of a child mesh must be coincident with a mesh line of the parent mesh. Figure 1 shows an example of two child meshes defined within a global parent mesh in computational space. This example shows a refinement in two mesh directions, however, the SDDMG method allows for refinement in a single direction.

Every subsequent level of mesh refinement is done in a similar manner. The child meshes on the previous mesh level are called parent meshes on their mesh level. From within these meshes, new child meshes are defined within the boundary of the parent mesh.

The information that is needed to facilitate communication between a child mesh and its parent mesh is the location of the child mesh within its parent mesh and the type of refinement strategy used to generate the child mesh. The location of the child mesh within its parent mesh is important as it determines the type of boundary conditions to be applied to the child mesh. If a child mesh boundary is coincident with an external boundary then the appropriate external boundary conditions is used. If the child mesh boundary is internal to the parent mesh, the appropriate interface condition is applied.

Multigrid Strategy. The present work used a multigrid to computationally link a child and parent mesh. Within the context of multigrid, a child mesh defines the fine mesh and the associated parent mesh the coarse mesh. The steps involved with multigrid [Brandt, 1977] are: an iteration procedure for solving the governing equations at each mesh level; a prolongation operator for transferring information from the parent mesh to the child mesh; a restriction operator for transferring information from the child mesh to the parent mesh. In the present work, a Runge-Kutta iteration procedure is used to advance the solution on each mesh level. A multigrid procedure also requires an estimate of relative truncation error between the child mesh and the associated parent mesh. This truncation error estimate appears as a forcing function in the mean flow equations associated with the parent mesh. Inclusion of the truncation error estimate in the mean flow equations associated with the parent mesh ensures that the spatial accuracy of these equations is consistent with the equations being solved on the child mesh. Further details on the multigrid strategy used in the present work can be found in Celestina [1999].

Mesh Generation Strategy. The domain decomposition approach presented here assumes that all meshes for a simulation are generated before the calculation is started. The primary reason for this is to preserve the integrity of the geometry, primarily the blade surface definition, across all mesh levels. The first step in this process is to generate a very fine mesh with uniform spacing for the entire computational domain using the mesh generation code developed by Mulac [1986]. In constructing the finest mesh, one must consider the distance from the solid surfaces defined in terms of boundary layer wall units y^+. This must be consistent with the wall function boundary conditions of the turbulence model. Of equal importance is adequate resolution of the leading edge and trailing edge regions of the turbomachine geometry. For transonic blading, the region over which a shock wave interacts with a boundary layer also requires fine resolution.

As was previously stated, the only direction in which the mesh is stretched is the radial direction. Uniform mesh spacing is maintained in the blade to blade direction.

The fine global mesh is used to generate the global parent mesh and all child meshes by discarding the appropriate number of mesh points from the fine global mesh. The effect of the mesh generation procedure on the definition of the leading edge region of a high-speed compressor rotor is shown in Figure 2. The global parent mesh, mesh level 1, generates a wedge-like leading edge. After five levels of mesh refinement, the finest child mesh, mesh level 6, provides a good definition of the leading edge region. The axial definition of mesh levels 3 and 4 are identical because they involve only a refinement in the pitch-wise direction.

Following the generation of all the parent and child meshes, a procedure is applied to all the sub-domain meshes to ensure that the interface mesh lines of a child mesh are coincident with a mesh line of the parent mesh. This procedure is important as it simplifies the specification of the interface boundary condition on the child mesh. The direction of the projected area of the child mesh at the interface is identical to the parent mesh and the value of the projected area is half that of the parent mesh.

Boundary Conditions. The external boundary conditions are applied at the boundary of the finest mesh, i.e., parent or child, coincident with the external boundary. At solid surfaces, the external boundary conditions require that there be no heat transfer and that the fluid velocity relative to the surface be zero. At the incoming flow boundary, the external boundary condition sets the fluid total temperature, total pressure and flow direction. At the exit of the flow domain, the external boundary condition sets the static pressure.

At the external boundary for all other mesh levels, the external boundary conditions incorporate terms which reflect the relative truncation error between the parent and child mesh. The details associated with the implementation of external boundary conditions can be found in Celestina [1999].

Interface Conditions. To complete the implementation of the domain decomposition procedure, the interface condition needs to be applied at a child mesh boundary not coincident with an external boundary. Thus these interface conditions are applied at the child mesh boundary coincident with a parent mesh surface. This is a line for two-dimensional flows and a plane for three-dimensional flows. The interface condition must conserve mass, momenta and energy across the interface between the child and parent mesh. The pressure must also be continuous across the interface. These requirements are stated by the following equations:

$$\begin{aligned} \rho_C &= \rho_P \\ [\rho\mathbf{v}]_C &= [\rho\mathbf{v}]_P \\ p_C &= p_P \\ H_{0C} &= H_{0P} \end{aligned} \tag{1}$$

where ρ is density, $\rho\mathbf{v}$ is the momentum vector, p is pressure and H_0 is the enthalpy.

Figure 3 shows an interface surface between two parent mesh cells. The upper parent cell is within a child mesh domain and contains four child mesh cells. The lower parent mesh cell is outside but adjacent to a child mesh domain and contains the child mesh "image" cells. The open circles in Figure 3 represent the center of the parent mesh cells and the open squares represent the center of the child mesh cells. The open broken line squares represent the center of the child mesh "image" cells. The physical location of the right-hand side of Equation (1) is represented by the shaded circle in Figure (1). The value of ρ, $\rho\mathbf{v}$, p, and H_0 at this location is the average of ρ, $\rho\mathbf{v}$, p, and H_0 from the centers of the parent mesh cells bordering the interface surface. The physical location of the left-hand side of Equation (1) is represented by the shaded squares in Figure 3. The value of ρ, $\rho\mathbf{v}$, p, and H_0 at these squares is set equal to the value of the corresponding variable located at the shaded circle.

The value of ρ, $\rho \mathbf{v}$, p, and H_0 at the cell center of the child mesh "image" cell is then obtained by linear extrapolation using the value at the child interface surface and the value of the center of the child mesh bordering the child interface surface. The "image" cell values along with the interior cell values are then used to compute the viscous stress at the interface surface.

Implementation. The solution procedure is illustrated in the schematic diagram in Figure 4, and the details can be found in Celestina [1999]. The calculation begins on a mesh denoted as GPM (Global Parent Mesh) in Figure 4. This mesh is covers the entire computational domain and represents mesh level I. The next mesh is the child of GPM and covers a portion of the computational domain. It should be noted that the child mesh domain may be identical to the parent mesh domain. This mesh represents mesh level II. A preset number of Runge-Kutta iterations, indicated as N iters. at the top of the diagram, are performed on GPM. The resulting estimate of the solution is interpolated, indicated as the broken line in the diagram, onto the child mesh (mesh level II). A preset number of iterations are performed on the child mesh. The updated estimate of the solution is passed back to the GPM along with an estimate of the relative truncation error associated with these two meshes. Once again, N iterations are performed on the GPM. The updated estimate of the solution is then passed back to the child mesh. This procedure represents a V-cycle multigrid solution strategy [Brandt, 1977].

The next level of mesh refinement is now introduced. The estimate of the solution from the child mesh, level II, is interpolated onto the next mesh level, level III. The child mesh, level II, becomes the parent mesh while the level III mesh becomes its child mesh. The Runge-Kutta iteration procedure is initiated on the new parent mesh. After a preset number of iterations, N iters., the estimate of the solution is interpolated onto mesh level III. A set number of Runge-Kutta iterations are performed at this mesh level. The updated estimate of the solution along with an estimate of the relative truncation error associated with the parent and child mesh is passed back to the parent mesh. A set number of Runge-Kutta iterations are performed on the parent mesh. At the completion of the iteration procedure, the parent mesh is redefined as a child mesh (Level II) associated with a parent mesh (GPM). The updated estimate of the solution from the redefined parent mesh is passed back to its parent along with an estimate of the relative truncation error. Once again, N Runge-Kutta iterations are performed on the parent mesh. Following a V-cycle multigrid strategy, the updated estimate of the solution is passed back to the child mesh, level II. At mesh level II, N Runge-Kutta iterations are performed and the subsequent estimate of the solution is passed onto the child mesh (mesh level III) of mesh level II. After a set number of Runge-Kutta iterations are completed on the child mesh, the procedure checks to see if there is another mesh level within mesh level III. If so, the mesh level is advanced and mesh level III becomes the parent mesh for mesh level IV. The above procedure is then repeated involving all the previously defined mesh levels. This procedure is continued until all of the predetermined mesh levels have been included. Upon inclusion of the last mesh level, the solution strategy is terminated when the change in the estimated solution (based on two successive passes through the solution strategy) is within a given tolerance.

If, upon examination of the converged solution, it is felt that more resolution is needed in a given flow region, a finer mesh can be generated spanning the region. This new mesh is introduced at the appropriate mesh level and the solution strategy restarted incorporating the new mesh. An example of this is discussed in the results section where two additional mesh refinements are added to a converged solution.

RESULTS

Two geometries are presented to test and validate the SDDMG method. The cases are: a compressor cascade and a turbine cascade. The geometry for the two cascade cases include solid end-walls. Both cases have a limited amount of experimental data available. Comparisons to this data are made where possible.

ARL Compressor. The ARL cascade [Zierke and Deutsch, 1989] is shown in Figure 5. This cascade is made up of double-circular-arc airfoils typical of a highly loaded compressor blade. From the test report, the chord length c is given as 228.6 mm and the cascade solidity is 2.14. The aspect ratio is 1.61. The incoming flow is subsonic with a velocity of 33 m/s and the Reynolds number based on airfoil chord is 501,000.

To limit the influence of side-wall and end-wall boundary layer growth on the measurements, suction was applied upstream of the cascade inlet plane on all walls. To simulate the test set-up, the AR of the simulated geometry was set to 8. This is done primarily to limit the impact of the side-wall and end-wall boundary layers on the core flow.

Since the geometry of the cascade airfoils is two-dimensional and the code used in this study is written in cylindrical coordinates, the hub and shroud, representing the cascade side-walls, must be placed at a very large radius. In addition, the ratio of the hub radius, R_h, and the shroud radius, R_s, must be near one. These two requirements yield a radius ratio $R^* = \frac{R_s - R_h}{R_s}$ near zero. In this study, the hub to shroud radius was set to 0.947 yielding a radius ratio of 0.053.

The test report presented data for three incidence angles.

The simulation will only consider the data presented for an incidence angle of -1.5^o.

The meshes used in the simulation of the ARL compressor cascade were of uniform spacing in the cascade plane. In the radial direction, the mesh spacing was non-uniform in order to resolve the side-wall boundary layers. The meshes on a cascade plane located at midspan are shown in Figure 6. A total of seven mesh levels are used in the present simulation with six sub-domain mesh levels. Table 1 gives a summary of the mesh sizes:

Mesh Level	Axial Points	Radial Points	Tangential Points	Number of Meshes
1	61	41	21	1
2	81	41	11	2
3	121	41	11	2
4	201	41	11	2
5	361	41	11	2
6	41	41	11	4
7	41	41	11	4

Table 1. SDDMG Mesh Refinement Schedule for ARL Compressor.

The global parent is Mesh Level 1 and contains 61 axial points with 21 of these points distributed uniformly along the chord of the airfoil. The inlet and outlet flow planes are set one chord length upstream and downstream, respectively, of the cascade inlet and exit planes. The number of radial mesh planes is fixed at 41. The spacing between these radial planes is varied in order to resolve the side-wall boundaries and is maintained for all sub-domain meshes. In the global parent mesh, 21 equally spaced planes are distributed across the cascade passage. The first set of subdomain refinements, mesh level II, starts at 50% chord upstream of the cascade inlet plane and ends at 50% chord downstream of the cascade exit plane. This refinement extends 25% of the pitch into the flow passage from either side of the blade surface. The third level of mesh refinement starts at 25% chord upstream of the cascade inlet plane and ends at 25% chord downstream of the cascade exit plane and extends 121/2% into the flow passage from either blade surface. This refinement strategy is repeated for the next two mesh levels with mesh level IV starting at 121/2% (half of 25%) upstream of the cascade inlet plane and ending at 121/2% (half of 25%) downstream of the cascade exit plane and extending half of 121/2% into the flow passage from either blade surface. Mesh levels 6 and 7 are used to refine the region of flow surrounding the leading edge and trailing edge. These two sub-domains are illustrated in Figures 7(a) and 7(b).

The simulation of the ARL cascade was done for an incidence angle of zero degrees. This incidence angle was established by matching the blade pressure distribution as predicted by a potential flow code [McFarland, 1982 and 1984] to that measured. It was felt that this procedure removed any issues associated with flow periodicity in the experiment.

Figure 8 shows contours of velocity magnitude at the midspan plane of the cascade. The contours of velocity magnitude remain continuous as they pass between the various mesh levels. The wake is seen to decay in a smooth manner with distance from the trailing edge. Figure 9 shows velocity vectors in the region of the suction surface trailing edge. The flow is separated from the suction surface in this region. The zero velocity line is shown in the figure and is seen going smoothly through two mesh levels with the separation region extending across three mesh levels. The smooth transition of the flow from one mesh level to another is a direct result of the multigrid procedure.

The SDDMG procedure can converge to a mesh independent solution in critical flow regions such as the region surrounding the leading edge. The pressure field in this region of flow controls the initial development of the blade boundary layers. Another flow region which is important to resolve is the region of flow near the suction surface of the blade trailing edge. The flow in this region plays a major role in establishing the flow blockage and the blade circulation. To show that the solution in the leading edge region for the ARL cascade is independent of mesh, the blade pressure distribution, in terms of a pressure coefficient, C_p, for the various mesh levels is plotted as a function of distance from the leading edge in Figure 10. This shows that as the mesh refinement is increased (level 1 being the coarsest and level 7 the finest), the surface pressure distribution asymptotes to a curve which is independent of mesh level, hence a mesh independent result. In addition, note that the distribution associated with all mesh levels coarser than the finest, level 7, appear to be "smooth" estimates of the fine mesh result. This being the case even for the coarsest mesh (level 1) in which leading edge is viewed as a wedge. These "smooth" estimates of the fine mesh result is a direct result of the multigrid strategy underpinning the SDDMG procedure.

Figure 11 shows the axial velocity plotted as a function of distance away from the suction surface for the finest 4 mesh levels. The chordwise location is near the suction surface trailing edge at about 90% of chord. The finest mesh is level 5 and the coarsest mesh is level 2. The velocity profiles obtained from the solution on each mesh level form a smooth velocity profile. The profiles on the finest two mesh levels, levels 4 and 5, are nearly identical and indicate that the solution in the region of the suction surface trailing edge is nearly mesh independent.

The next two figures show comparisons with experimental data. Figure 12 shows the blade surface pressure distribution as a function of blade chord as computed and measured. As noted above, the incidence angle for the simulation is zero degrees while that reported by Zierke and Deutsch [1989] is −1.5 degrees. The difference compensates for incoming flow differences between the simulated cascade with an infinite number of blades and the cascade in the experiment whose blade count is five. The agreement between the simulation result and the experiment is excellent. The final result for the ARL cascade, Figure 13, shows the profile of the axial velocity across the pitch of the cascade. The axial location is 32.9% of the chord downstream of the cascade exit plane. Both simulation results and measurements are shown in Figure 13. The simulation results incorporated all seven mesh levels. The agreement between the simulation results and measurement are excellent. Since it was shown that the simulation results are nearly independent of mesh, the difference between measurement is due to geometric differences between the physical cascade test setup and that specified in the simulation, experimental error, or errors introduced by the turbulence model.

VKI Turbine Cascade. The VKI turbine cascade airfoil geometry is shown in Figure 14. It is representative of a highly loaded turbine nozzle. The aerodynamic performance [Arts, *et al.* 1990] of a cascade of these airfoils was assessed in the Von Karman Institute short duration Isentropic Light Piston Compression Tube facility. The chord length of the tested airfoils is 67.647 mm and the cascade solidity is 1.176. Additional details of the cascade geometry can be found in Arts, *et al.* [1990]. All simulations were performed for an isentropic exit Mach number of 0.85. The experimental setup did not allow for the removal of the side wall boundary layers. Thus the cascade is simulated with the side walls included. Thus, the simulation is three-dimensional.

A cascade plane perspective of the midspan mesh used in the initial simulation is shown in Figure 15. On each cascade plane, the mesh has seven mesh levels. These submeshes are identical for all cascade planes. In the spanwise direction, there are 41 cascade planes. They are spaced in the spanwise direction so as to resolve the side wall boundary layers.

Table 2 gives a summary of the mesh sizes:

Mesh Level	Axial Points	Radial Points	Tangential Points	Number of Meshes
1	61	41	21	1
2	81	41	11	2
3	121	41	11	2
4	101	41	11	2
5	101	41	11	2
6	21	41	11	4
7	21	41	11	4

Table 2. SDDMG Mesh Refinement Schedule for VKI Turbine.

Mesh level 1 is the global parent mesh. The first two mesh levels, levels 2 and 3, are axial and pitchwise refinements of the global parent mesh. Mesh levels 4 and 5 are pitchwise refinements only and are employed to resolve the blade boundaries. Finally, mesh levels 6 and 7 are designed to better define the flow in the neighborhood of the leading and trailing edge.

A series of simulations showed that the flowfield was two-dimensional between 10% and 80% of span and thus only results for the midspan cascade plane will be reported. Figure 16 is a plot of the Mach number contours at midspan. The contours remain continuous as they pass through the various mesh levels. Figure 17 shows the velocity vectors in the region of the blade trailing edge. There is no evidence of these velocity vectors being discontinuous. Indeed, one can clearly see two counter-rotating vorticies formed by the merger of the flow the suction and pressure surface.

A plot of the local loss coefficient, defined as

$$\chi = \frac{1 - \frac{p_2}{p_{t_2}}^{\frac{\gamma-1}{\gamma}}}{1 - \frac{p_2}{p_{t_1}}^{\frac{\gamma-1}{\gamma}}} - 1$$

where p is pressure, p_t is the total pressure and the indice 1 denotes the inlet flow plane and 2 the measuring plane at 142% chord downstream of the cascade inlet plane is shown as a function of pitch in Figure 18. Both simulation and experimental results are shown. The agreement appears good, however, the simulation results overpredict the loss at the center of the wake. To ascertain whether this overprediction of loss is numerical in origin, a further refinement of the flow neighboring the suction surface was attempted. At the location of minimum suction surface pressure, the mesh refinement reduced the value of y^+ at the centroid of the first cell from approximately 75 to approximately 20. The resulting velocity profile through the suction surface boundary layer is shown in Figure 19. Shown on the figure are plots associated with the three mesh levels. The finest mesh is level 9 and the coarsest mesh is level 5. Mesh level 8 represents the first refinement of mesh level 5. The plots on Figure 19 show that the results for mesh levels 8 and 9 are nearly identical. This indicates that the solution through the suction surface boundary layer in the vicinity of minimum pressure is nearly mesh independent. The simulation results presented in Figure 18 are associated with the velocity profile for mesh level 5. Note that the results for mesh level 5 fail to resolve the outer region of the suction surface boundary layer. The impact of the refined definition of the suction surface boundary layer on the local loss coefficient is shown in Figure 20 as a function of pitch. The plots from

Figure 18 are repeated in the figure. The added refinement appears to have little impact on the estimated loss at the center of the wake. The refinement does appear to yield a sharper loss profile with the loss profile for level 8 being nearly that for mesh level 9. Thus one can state that the loss profiles are nearly mesh independent. Any differences between the simulation and experimental result is due to experimental error (note the experimental loss coefficient is greater than one in the core flow region), a difference between the simulated geometry and that of the experiment, or the modeling of turbulence.

For both the ARL and VKI cascade simulations, the SDDMG procedure did not adversely impact the stability of the Runge-Kutta iteration strategy. On the contrary the stability of the Runge-Kutta procedure appeared to be improved by the SDDMG procedure. This positive impact on stability appears to be related to the elimination of the adverse effects of mesh stretching by the SDDMG procedure.

SUMMARY AND CONCLUSIONS

Accurate predictions of the aerodynamic performance of turbomachinery blading requires resolution of flow features near the leading and trailing edges of blades, boundary layers and clearance flows. To obtain the required flow detail, grid cells are clustered in regions of high flow gradients and then stretched to fill in the remaining flow region. This often results in grids with very high aspect ratios. For CFD codes which employ a Runge-Kutta based iteration stategy, this often leads to numerical stability problems. To circumvent these stability problems and still have the ability to resolve features associated with high flow gradients, a segmented domain decomposition multigrid (SDDMG) procedure was developed. The SDDMG procedure was implemented in 2D to tests its ability to produce grid independent solutions and enhance the stability of a Runge-Kutta based interation stategy.

The SDDMG procedure was used to simulate a compressor and turbine cascade. Each case was used to show a different feature of the SDDMG procedure. Both simulations yield results which were grid independent. Results were shown that illustrated the ability of the SDDMG procedure to capture the flow details in the neighborhood of a compressor blade leading edge and a turbine blade trailing edge. In addition, it was shown that the SDDMG procedure yielded velocity profiles associated with blade boundary layers which were grid independent.

Comparison of simulation results to expermental data showed the SDDMG procedure was predicting solutions that are consistent with the experimental data. Indeed since the simulation results are, for all practical purposes grid independent, any difference between simulation and experiment is due to geometry differences, experimental error, or the modeling of turbulence.

Based on the results from this study the SDDMG procedure is a viable alternative to grid stretching to resolve the flow features which control the performance of turbomachinery blading. An implementation of the SDDMG procedure in 3D is recommended.

REFERENCES

Adamczyk, J. J., Celestina, M. L., Beach, T. A., Barnett, M., "Simulation of Three-Dimensional Viscous Flows Within a Multistage Turbine," *J. of Turbomachinery*, V. 112, N. 3, July, 1990, pp. 370-376.

Arts, T., Lambert de Rouvroit, M., and Rutherford, A. W., "Aero-thermal Investigation of a Highly Loaded Transonic Linear Turbine Guide Vane Cascade," VKI Technical Note 174, 1990.

Berger, M. J. and Colella, P., "Local Adaptive Mesh Refinement for Shock Hydrodynamics", *Journal of Computational Physics*, **82**, pp. 64-84, 1989.

Brandt, A., "Multi-Level Adaptive Solutions to Boundary-Value Problems," *Mathematics of Computation*, V. 31, N. 138 April, 1977, pp. 333-390.

Celestina, M., "Segmented Domain Decomposition Multigrid for 3-D Turbomachinery Flows", *Ph.D. Disseration*, Department of Aerospace Engineering and Engineering Mechanics, University of Cincinnati, 1999.

Launder, B. E., and Spalding, D. B., "The Numerical Computation of Turbulent Flows," *Comp. Math. Appl. Mech. Engr.* V. 3, 1974, pp. 269-289.

Liou, M.-S., and Kao, K.-H., "Progress in Grid Generation: From Chimera to DRAGON Grids", *NASA TM 106709*, 1994.

McFarland, E. R., "Solution of Plane Cascade Flow Using Improved Surface Singularity Methods," *J. of Engr. for Power*, V. 104, July, 1982, pp. 668-674.

McFarland, E. R., "A Rapid Blade-to-Blade Solution for Use in Turbomachinery Design," *J. of Engr. for Gas Turbines and Power*, V. 106, April, 1984, pp. 376-382.

Mulac, R. A., "A Multistage Mesh Generator for Solving the Average-Passage Equation System," *NASA CR-179539*, 1986.

Shabbir, A., Zhu, J., and Celestina, M. L., "Assessment of Three Turbulence Models in a Compressor Rotor", ASME 96-GT-198, 1996.

Srinivasan, K. and Rubin, S. G., "Solution Based Grid Optimization Through Segmented Multigrid Domain Decomposition," *J. Comp. Phys.*, V. 136, N. 2, Sept., 1997. pp. 467-493.

Steger, J., and Benek, J. A., "On the Use of Composite Grid Schemes in Computational Aerodynamics", *Computer Methods in Applied Mechanics and Engineering*, Vol. 64, pp. 301-320, 1987.

Zierke, W. C., and Deutsch, S., "The Measurement of Boundary Layers on a Compressor Blade in Cascade, Volume 1," NASA CR-185118, 1989.

ACKNOWLEDGMENTS

The first author wishes to thank Rick Mulac for his help with grid generation and Aamir Shabbir for help with the implementation of the $k - \epsilon$ turbulence model in this work.

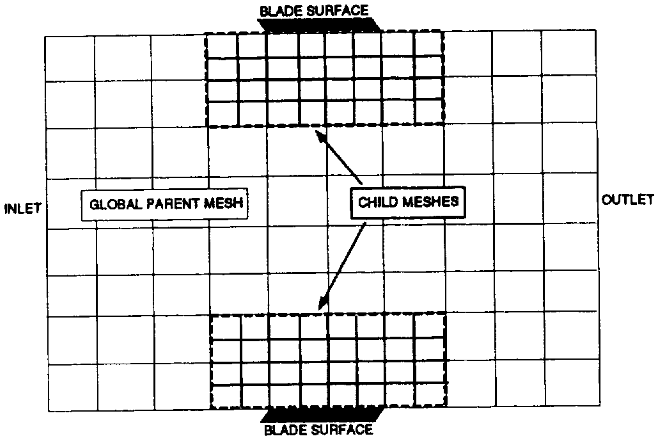

Fig. 1. Global parent mesh with two child meshes in computational coordinates. The dashed line depicts the boundaries of the child meshes.

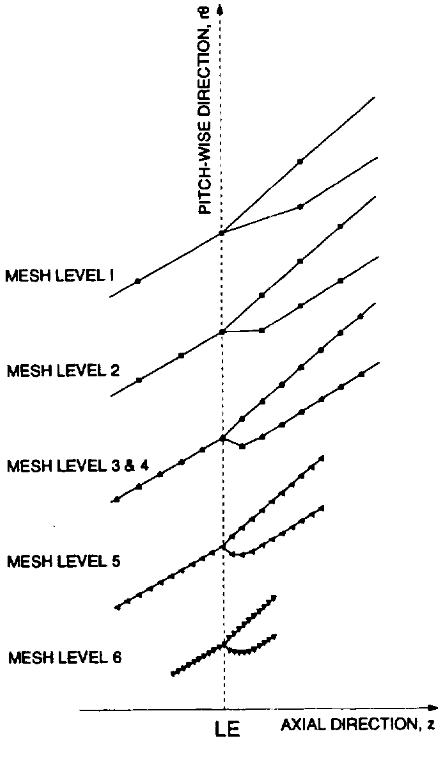

Fig. 2. Resolution of blade surface definition with mesh refinement.

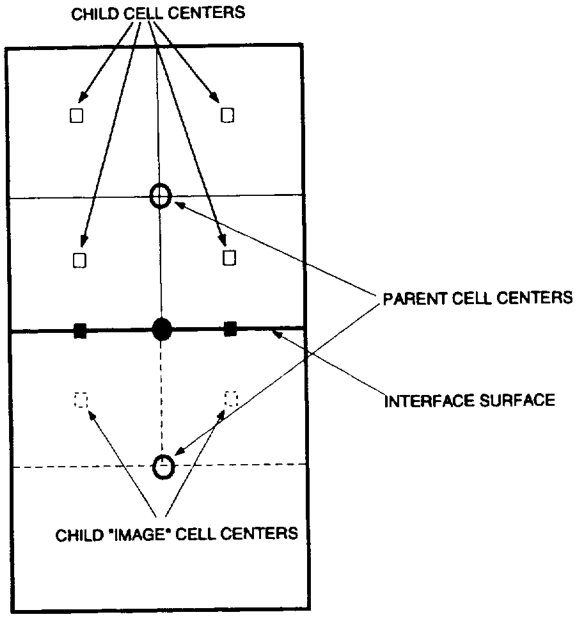

Fig. 3. Schematic of a parent mesh / child mesh interface surface.

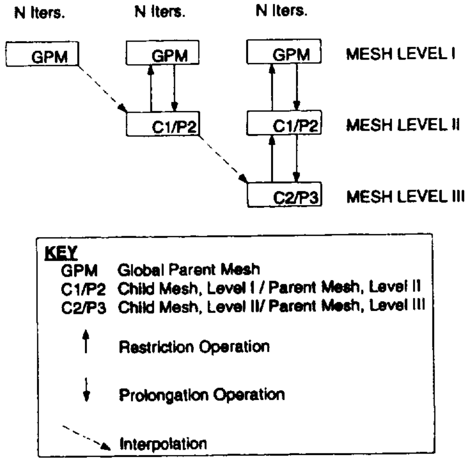

Fig. 4. Schematic of SDDMG procedure.

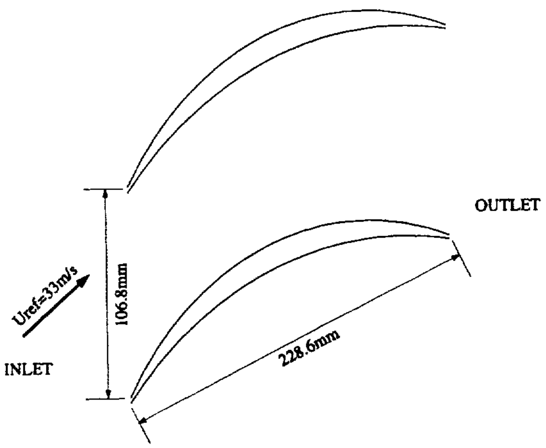

Fig. 5. Schematic of the ARL Compressor Cascade.

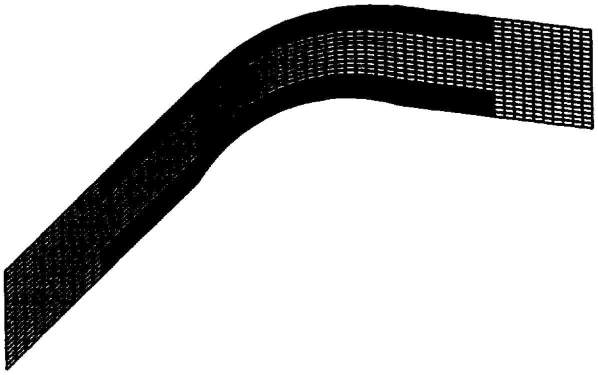

Fig. 6. Sectional view of the ARL compressor SDDMG mesh at midspan with 7 mesh levels.

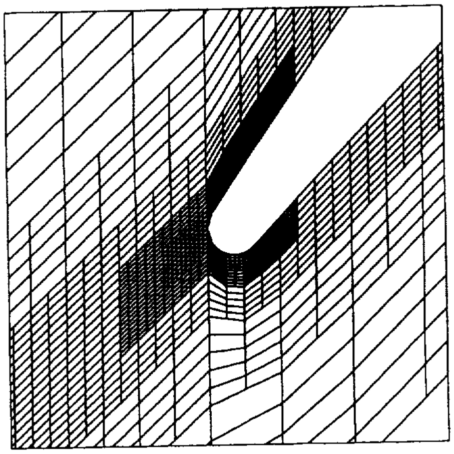

Fig. 7(a). SDDMG mesh near the leading edge region of the ARL compressor at midspan.

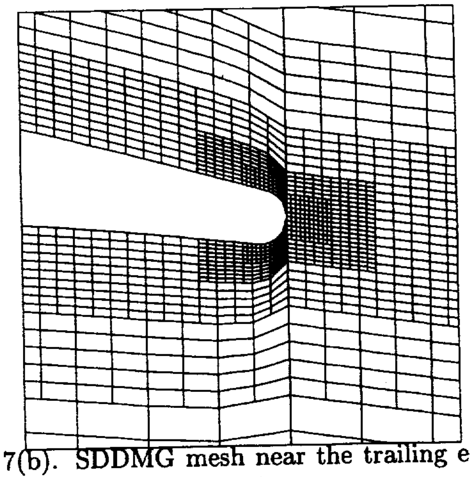

Fig. 7(b). SDDMG mesh near the trailing edge region of the ARL compressor at midspan.

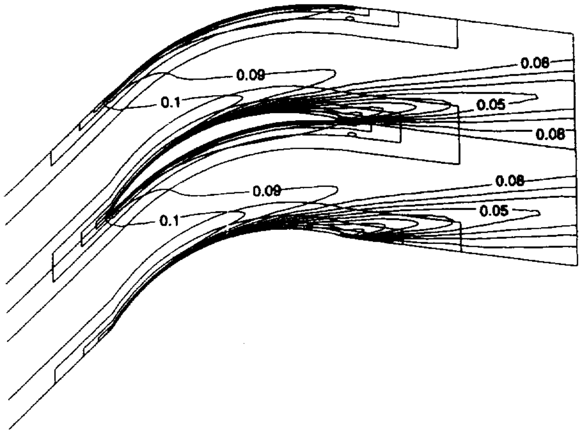

Fig. 8. Contours of velocity magnitude at midspan.

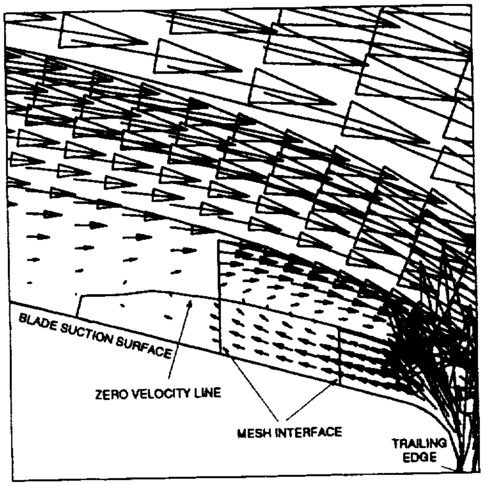

Fig. 9. Velocity vectors near the suction surface trailing edge midspan for SDDMG.

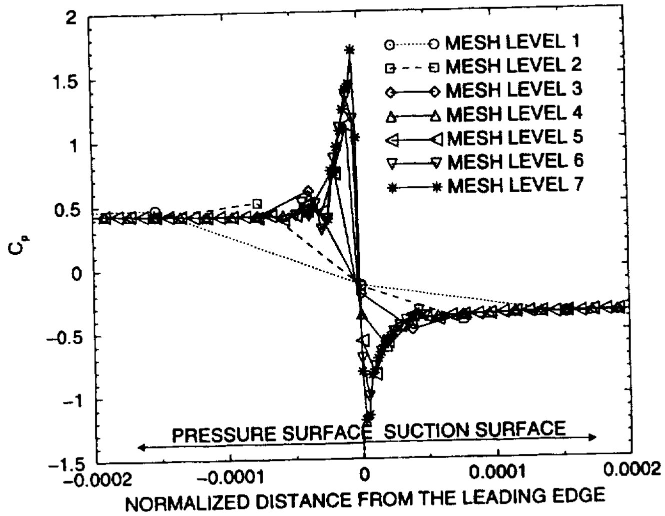

Fig. 10. Convergence of Blade Surface C_p for all the SDDMG mesh levels vs. normalized distance from the leading edge at midspan.

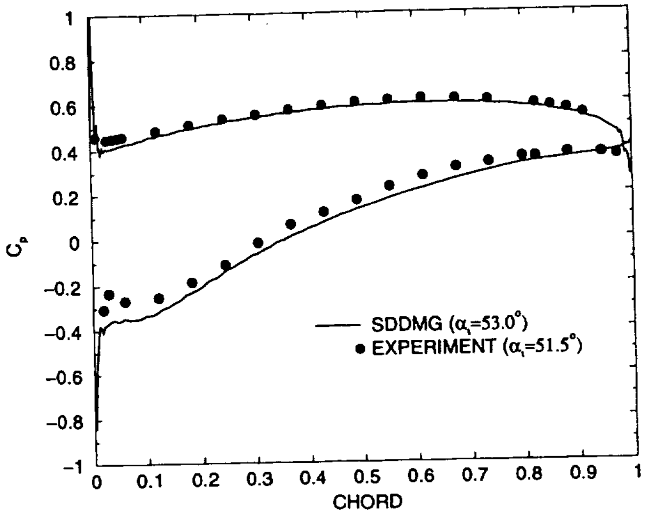

Fig. 12. Comparison of Blade Surface C_p vs. percent chord at midspan for experimental data and SDDMG.

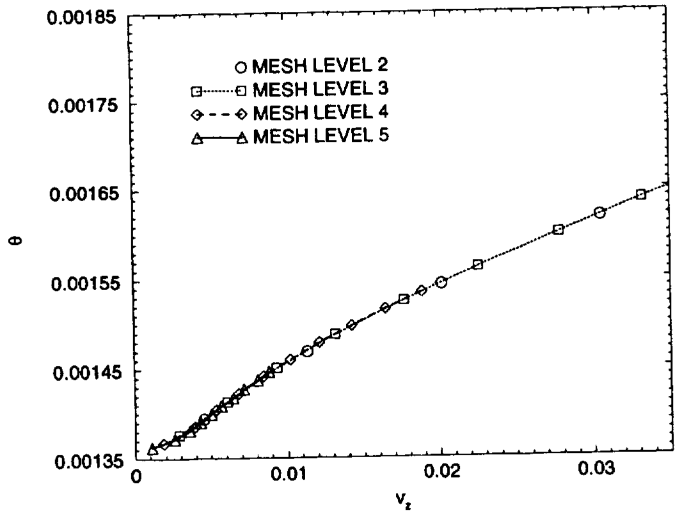

Fig. 11. v_z versus θ on suction surface at midspan. ARL compressor cascade.

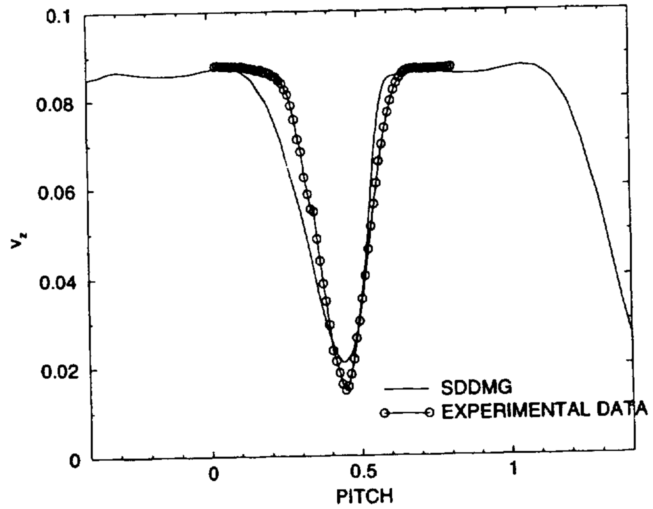

Fig. 13. Comparison of axial velocity, v_z vs. pitch at midspan for SDDMG and experimental data.

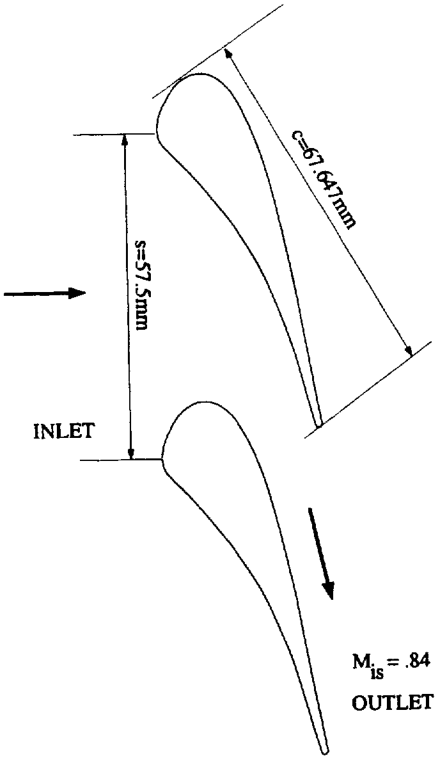

Fig. 14. Schematic of VKI Turbine Cascade.

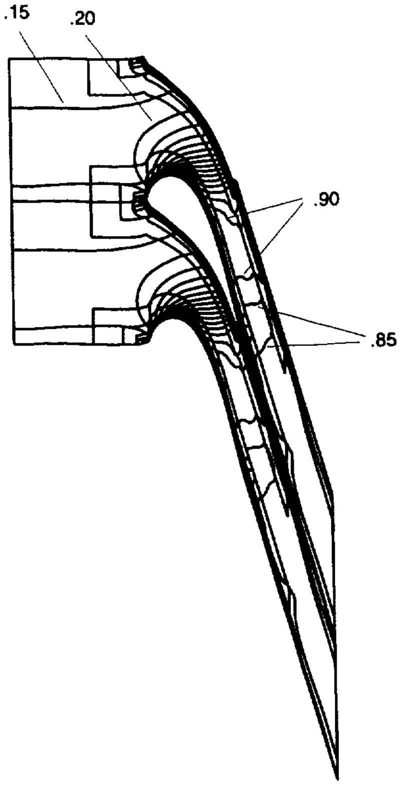

Fig. 16. Mach Number contours at midspan in increments of 0.05.

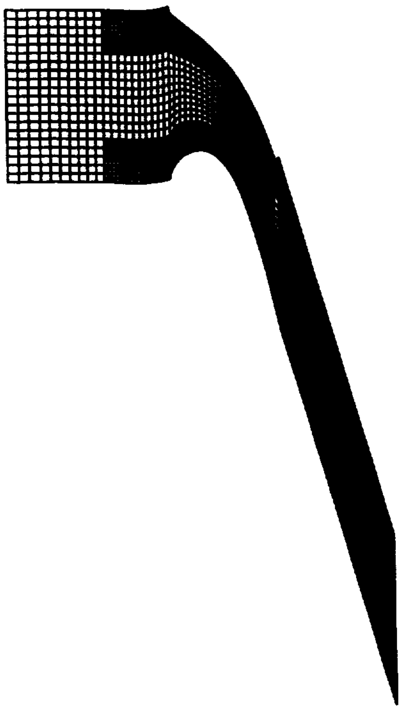

Fig. 15. Sectional view of the VKI turbine SDDMG mesh at midspan with 6 mesh levels.

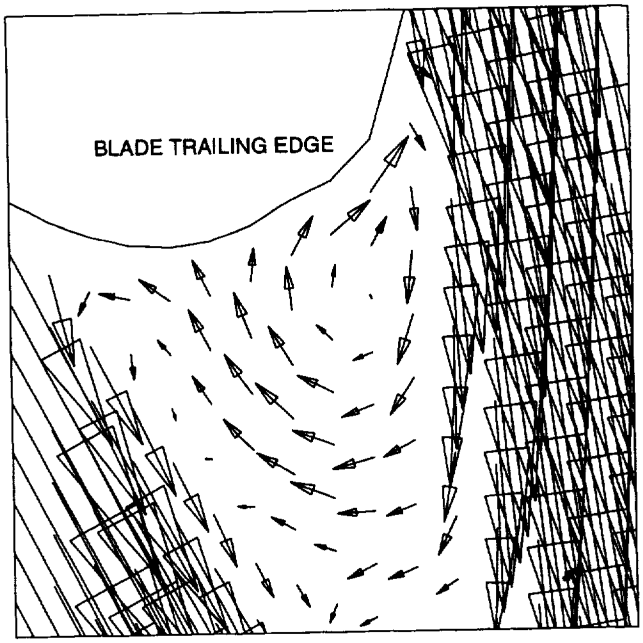

Fig. 17. Flow vectors near the trailing edge at midspan.

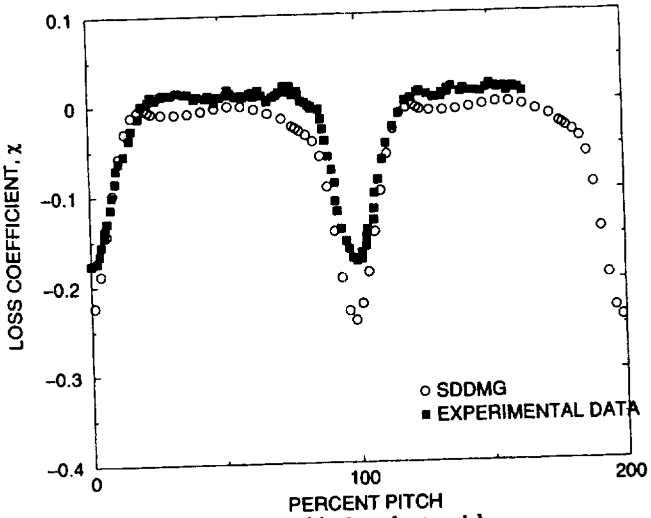

Fig. 18. Loss coefficient at 143% chord at midspan.

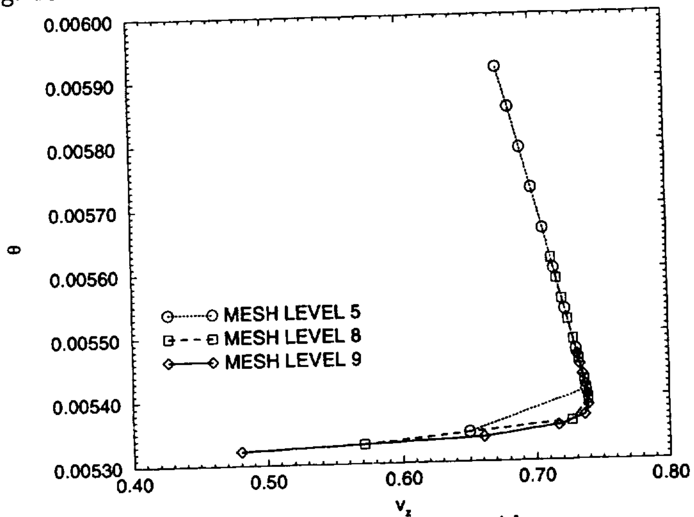

Fig. 19. v_z versus θ on suction surface at midspan.

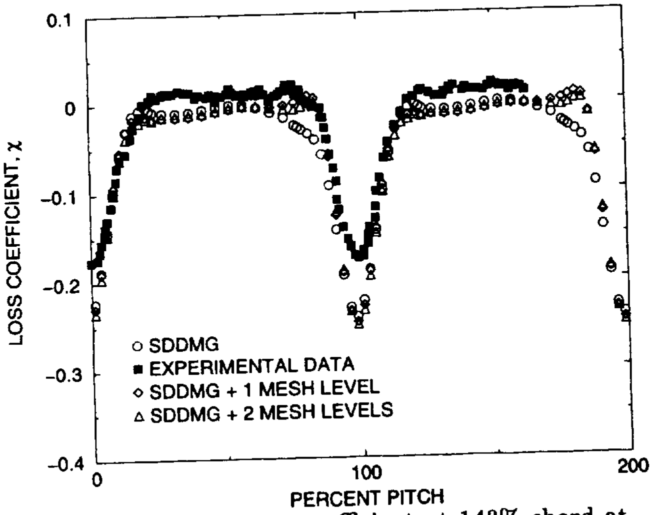

Fig. 20. Comparison of Loss coefficient at 143% chord at midspan.